

The effect of seafloor roughness on passive estimates of the seabed reflection coefficient

Derek R. Olson^{a)} 

Oceanography Department, Naval Postgraduate School, Monterey, California 99343, USA

ABSTRACT:

In this work, a model is developed for the effect of seafloor interface roughness on passive estimates of the reflection coefficient. The main result is an expression for the total intensity reflection coefficient, with separate coherent and incoherent contributions. Assumptions of this model include constant sound speed in the ocean, stationary and Gaussian seafloor roughness, and ambient noise. Numerical examples for the coherent, incoherent, and total contributions to the intensity reflection coefficient are presented for halfspace and layered environments—all using the small slope approximation. To illustrate the potential parameter errors that results from using a flat interface wave model when roughness is present, a geoacoustic inversion is performed using the proposed model as input data. A joint roughness-geoacoustic inversion of simulated data using the proposed model was also performed. It was found that the true roughness and geoacoustic parameters can be inverted using this model, but the sensitivity to the outer scale of the rough surface has the highest error compared to the other parameters.

<https://doi.org/10.1121/10.0016846>

(Received 5 October 2022; accepted 12 December 2022; published online 26 January 2023)

[Editor: Stan E. Dosso]

Pages: 586–601

I. INTRODUCTION

The reflection coefficient of the seafloor contains a great deal of information about its layering structure, more specifically, its geoacoustic properties—the sound speed, density, and attenuation of its layers, and their sizes (Dettmer *et al.*, 2010; Holland and Dettmer, 2013). Inverse techniques based on Bayes' theorem have been extensively employed to extract this information from both active (Ballard *et al.*, 2018; Dettmer *et al.*, 2010) and passive (using ambient sound) estimates of the reflection coefficient (Quijano *et al.*, 2013, 2012). The passive technique has advantages because it does not require an active source and has low environmental impact, and has recently become popular for remote sensing of the ocean interior and boundaries (Brooks and Gerstoft, 2009; Godin *et al.*, 2014; Li *et al.*, 2020, 2021; Woolfe *et al.*, 2015; Zhou *et al.*, 2022).

In the presence of roughness, the measured reflection coefficient can be altered compared to the flat interface case (Eckart, 1953; Jackson and Richardson, 2007), due to sound scattered away from the specular direction. This alteration can cause a mismatch between inverted geoacoustic properties and the true properties if a flat interface model is used in the inversion. A common way of incorporating the effect of roughness is to use the Kirchhoff approximation (Eckart, 1953), to calculate the coherent reflected field. In this approximation, the magnitude of the mean of the complex reflection coefficient, $|R_c(\theta)|$, is

$$|R_c(\theta)| = R_{\text{flat}}(\theta)e^{-2k^2h^2\sin^2\theta}, \quad (1)$$

where R_{flat} is the flat-interface reflection coefficient, the exponential term is known as the Eckart factor, and $kh \sin \theta/2$ is the Rayleigh parameter. Here, k is the acoustic wavenumber in water and h is the root mean square (rms) interface height. The coherent reflection coefficient takes into account the loss of coherent energy in the specular direction due to energy scattered into other angles when the incident field is composed of a monochromatic plane wave. Use of the coherent reflection coefficient is appropriate for comparison to measurements of the mean complex pressure (i.e., a coherent average) over independent areas of the seafloor. Layered seafloors have a much more complicated relationship between the rms roughness and the coherent reflection coefficient (Jackson and Olson, 2020).

Backscattering measurements have also been performed in conjunction with reflection measurements, for the purposes of remote sensing both roughness and geoacoustic properties, using a controlled active source and a directive receiver array (Steininger *et al.*, 2013). These types of measurements are highly informative, because the reflection coefficient and scattering cross section are influenced by roughness and the geoacoustic properties in different ways and can provide complimentary information. However, the work by Steininger *et al.* (2014) and Steininger *et al.* (2013) used inconsistent assumptions regarding the reflected and scattered field. Namely, it was assumed that the reflected field was unaffected by interface roughness, whereas energy conservation requires that the specular field be altered due to the backscattered energy that was measured. Forward modeling using the Langston-Kirchhoff was used to analyze active reflection measurements from a complicated inner

^{a)}Electronic mail: derek.olson@nps.edu

shelf area in with a layered seafloor with rough interfaces (Holland *et al.*, 2017). The assumptions used in this forward modeling were consistent, but no inversion was present because the model used was only applicable to individual realizations of seafloor roughness.

The concepts of coherent reflection coefficient and scattering cross section are quite useful when the incident field is produced by a coherent source with a narrow beam pattern (or the incident field has a well-defined direction and is measured by a system that can resolve directions). In measurements using ambient sound (particularly using wind-generated sound) the coherent reflection coefficient and scattering cross section are not directly observable quantities. First, the source is incoherent, meaning that the phase relationship between the incident (downgoing components) and reflected waves (upgoing components) is unknown. Second, the average over areas of the seafloor takes place incoherently. Last, passive measurements use incident fields that are composed of a continuum of plane wave directions (Kuperman and Ingenito, 1980).

In this work, a model is developed for the effect of roughness on passive measurements of the reflection coefficient. The analysis is based on using a known incident down-going spectrum (measured by an array) and employs the T-matrix for the relationship between the downgoing and upgoing plane wave components. This matrix contains all information regarding reflection and scattering from a heterogeneous seafloor [Jackson and Richardson (2007), Appendix J]. The following assumptions are made here: (1) the water column has a constant sound speed with no attenuation, (2) the noise field is produced by a diffuse sources near the surface (i.e., no discrete sources such as ships, or noncoherent sources such as thermal noise), (3) the reflection coefficient can be estimated by the ratio of the upward to downward noise intensity in a given beam (which is related to the first assumption), and (4) the roughness and noise field are both stationary random fields with zero mean. This model could be used to analyze data collected at sea, for example, within the commonly used Bayesian approach that is commonly used (Ballard *et al.*, 2018; Dettmer *et al.*, 2010; Quijano *et al.*, 2012). For environments with variable sound speed profiles and attenuation, geoacoustic inversion requires more detailed modeling of the noise covariance matrix, which was discussed by Muzi *et al.* (2015), Siderius and Gebbie (2019), and Siderius *et al.* (2010). The model developed in the present work could be extended to more realistic environments in future work.

A related problem has been studied by Voronovich (1999) (Chap. 7), who derived expressions for the pressure covariance in a stratified waveguide with a rough sea surface and a flat bottom using distributed surface noise sources and the diffusion approximation. That analysis was focused on the covariance and used a rough sea surface and flat seafloor. For the work presented here, the mathematics is considerably simplified compared to Voronovich's work due to the ability to estimate plane wave components with vertical line array. Additionally, the focus here is on the role of seabed roughness.

This paper is organized as follows. In Sec. II, the basic concepts necessary for the model derivation are presented. In Sec. III, the model for the effect of roughness scattering on the reflection coefficient is derived. In Sec. IV some numerical examples of the model for different environments and roughness parameters are given. In Sec. V, two examples of inverse methods are performed. First the effects of roughness on inversion are demonstrated by fitting a flat interface model to simulated data generated using the proposed model. Second, the proposed model is used both as simulated data and forward model to perform a joint roughness-geoacoustic inversion to demonstrate the feasibility of recovering roughness parameters using passive techniques. Conclusions are given in Sec. VI.

II. BASIC DEFINITIONS

In this section, the environment of the problem, as well as a few basic concepts necessary for the model derivation are presented. Following the convention used by Jackson and Richardson (2007), boldface capital letters are two dimensional vectors. The sound speed in the isovelocity water column is c_w . The frequency is f and $k = 2\pi f/c_w$. Consequently, k is constant in the water column. Let the downgoing Fourier amplitude of plane waves be defined by $\Psi^-(\mathbf{K})$, where $\mathbf{K} = (K_x, K_y)$ is the horizontal wave vector. The downgoing plane wave spectrum will be called the incident spectrum. The grazing angle given by this vector is calculated by

$$\theta = \cos^{-1}\left(\frac{K}{k}\right), \tag{2}$$

where $K = |\mathbf{K}| = \sqrt{K_x^2 + K_y^2}$ is the magnitude of the horizontal wavenumber.

It is assumed that the passive array results in a good estimate of Ψ^- , although this may not be a good assumption for very low noise levels. The effect of the beam response on this model could easily be included, e.g., using the formulas presented in Clark (2007) for the measured beam noise, given knowledge of the true ambient sound field and the array response. An ideal beam response is assumed here for simplicity.

Interaction with the seafloor produces an up-going plane wave complex amplitude spectrum, $\Psi^+(\mathbf{K})$, which is referred to as the scattered spectrum. For scattering from interface roughness, or volume heterogeneities, the incident and scattered plane wave spectra are connected through the T-matrix [Jackson and Richardson (2007), Appendix J],

$$\Psi^+(\mathbf{K}_s) = \iint \Psi^-(\mathbf{K}_i) T(\mathbf{K}_s, \mathbf{K}_i) d^2 K_i. \tag{3}$$

The T-matrix is the transfer function connecting the amplitude and phase of incident and scattered plane wave components. This relationship assumes a single interaction between the incident field and scattered field, which is consistent with the assumptions of passive reflection estimates (Harrison and Simons, 2002; Muzi *et al.*, 2015). In general,

the rough interface may have a significant impact on the directionality of the ambient sound field [Voronovich (1999), Chap. 7], but in this work the only concern is with the intensity ratio between the up and downgoing plane wave components.

Although the T-matrix can be used to characterize the scattered field from both roughness and volume heterogeneities, attention is restricted here to interface roughness. Let the vertical deviation of the rough interface from a horizontal plane be specified by $\zeta(\mathbf{R})$, where $\mathbf{R} = (x, y)$ is the 2D horizontal coordinate vector. The rough interface is assumed to be centered at the mean water depth, so we may treat it as a zero-mean random field. The rough interface is assumed to follow a Gaussian distribution and exhibit wide-sense stationarity. Therefore, it is completely characterized by its auto-covariance function and power spectral density. Let the 2D Fourier transform of $\zeta(x, y)$ be

$$Z(\mathbf{K}) = \frac{1}{(2\pi)^2} \int_{-\infty}^{\infty} \int_{-\infty}^{\infty} \zeta(x, y) e^{i(k_x x + k_y y)} dx dy. \quad (4)$$

Then, the power spectrum, $W(\mathbf{K})$, is defined by

$$W(\mathbf{K}) \delta(\mathbf{K} - \mathbf{K}') = \langle Z(\mathbf{K}) Z^*(\mathbf{K}') \rangle. \quad (5)$$

The rms height, h of the interface is defined by

$$h^2 = \langle |\zeta(x, y)|^2 \rangle = \int_{-\infty}^{\infty} \int_{-\infty}^{\infty} W(\mathbf{K}) d^2 K. \quad (6)$$

A specific form of the power spectrum is used when presenting numerical results (in Sec. IV), called the von Kármán spectrum. This model is horizontally isotropic, and defined by

$$W(K) = \frac{w_2}{(L_0^{-2} + K^2)^{3/2}}, \quad (7)$$

where w_2 is the spectral strength and sets the overall level of the spectrum. L_0 is the outer scale and sets the largest length scale of the power law surface. In general, this spectral form raises the denominator of Eq. (7) to the power of an exponent, $\gamma/2$, but γ is set to 3 in this model. This restriction is made so that the recently developed fast series approximation for the Kirchhoff integral (which enables the use of the small slope approximation) can be used, since the series approximation has only been used for $\gamma=3$. The von Kármán model is commonly used for natural rough surfaces, which typically exhibit power-law behavior at high wavenumbers (Brown and Scholz, 1985). The outer scale determines the location in wavenumber space at which the model transitions from a power-law at high wavenumbers to a constant at low wavenumbers. This location is $K_0 = L_0^{-1}$, and is used to parameterize the outer scale hereafter. Note that L_0 is not analogous to a correlation length or length scale that is used in the Gaussian roughness spectrum (Thorsos, 1988), since power law roughness is multiscale.

An important parameter of the rough interface is its mean square value, h^2 , which is given by [Jackson and Richardson (2007), Appendix D]

$$h^2 = \frac{2\pi w_2}{K_0}. \quad (8)$$

The non-dimensional parameter kh will be used extensively in the numerical examples given later. Large values of kh indicate significant scattering, and small values indicate less significant scattering. The degree of incoherent scattering, vs coherent reflection can be evaluated for simple cases using the Rayleigh factor. For this work, it will be quantified by the incoherent and coherent contributions to the total reflection coefficient, models for which are derived in Sec. III. Similarly, the dimensionless inverse outer scale will be denoted K_0/k .

The sediment geoacoustic properties consist of the sound speed, density, and attenuation. If the sediment contains layers, then layer thickness is used as well. These properties are parameterized using ν for the sound speed ratio between the sediment and water, a_ρ for the density ratio between the sediment and the water, and α as the sediment attenuation in dB/m/kHz. Layer thickness is denoted as d .

III. MODEL DEVELOPMENT

In passive estimates of seabed reflection for an isovelocity ocean, the goal is to measure the ratio of average downgoing intensity of the ambient sound field at a given angle to the average upgoing intensity at that same angle. The purpose of this section is to derive an expression for this ratio in terms of the scattering cross section, coherent reflection coefficient, and downgoing plane wave intensity.

The amplitude ratio between the downgoing and upgoing plane wave components is

$$R^P(\mathbf{K}) = \frac{\Psi^+(\mathbf{K})}{\Psi^-(\mathbf{K})}. \quad (9)$$

Since the incident field is a zero-mean random variable, and the rough interface is also assumed to be random, the first moment of the field is zero. The second moment is used instead, and requires two formal averages, one over the incident field, the other over the roughness realizations. This second moment is expressed by

$$\langle \langle R^P(\mathbf{K}) R^{P*}(\mathbf{K}') \rangle_{\Psi^-} \rangle_f = \frac{\langle \langle \Psi^+(\mathbf{K}) \Psi^{+*}(\mathbf{K}') \rangle_{\Psi^+} \rangle_f}{\langle \langle \Psi^-(\mathbf{K}) \Psi^{-*}(\mathbf{K}') \rangle_{\Psi^-} \rangle_f}, \quad (10)$$

where the subscripts on the brackets indicate the random variable over which the average is taken. The denominator only has a single average because we assume that the downgoing plane wave spectrum is accurately measured by the vertical line array. The downgoing components will be affected by scattering (due to multiple interactions with the seabed for distant noise sources), but we are concerned with the ratio rather than the total ambient noise field. This assumption is consistent with the standard assumptions of passive reflection measurements (Harrison and Simons, 2002; Muzi et al., 2015). The second moment written above is general enough that it takes into account cross-beam

coherence, i.e., $\langle \Psi^-(\mathbf{K})\Psi^-(\mathbf{K}') \rangle$, but the most general form is not analyzed here. The downgoing plane wave spectrum is characterized using

$$\langle |\Psi^-(\mathbf{K})|^2 \rangle_{\Psi^-} = D^-(\mathbf{K}), \tag{11}$$

where $D^-(\mathbf{K})$ is the mean pressure squared for each plane wave component (i.e., grazing angle) of the downgoing plane wave spectrum, and is typically estimated using a vertical line array.

A specific form for the numerator of Eq. (10) can be calculated using the definition of the T-matrix, Eq. (3) and restricting to the case $\mathbf{K}' = \mathbf{K}$, resulting in

$$\begin{aligned} & \langle \langle \Psi^+(\mathbf{K})\Psi^{+*}(\mathbf{K}) \rangle \rangle_{\Psi^-} \\ &= \iiint \langle \Psi^-(\mathbf{K}_i)\Psi^{-*}(\mathbf{K}_i) \rangle \\ & \times \langle T(\mathbf{K}, \mathbf{K}_i)T^*(\mathbf{K}, \mathbf{K}_i') \rangle d^2K_i d^2K_i'. \end{aligned} \tag{12}$$

To simplify this result, we define the total second moment of the T matrix as

$$C(\mathbf{K}, \mathbf{K}', \mathbf{K}_i, \mathbf{K}_i') = \langle T(\mathbf{K}, \mathbf{K}_i)T^*(\mathbf{K}', \mathbf{K}_i') \rangle. \tag{13}$$

The total second moment can be split into a coherent component,

$$C_c = \langle T(\mathbf{K}, \mathbf{K}_i) \rangle \langle T(\mathbf{K}', \mathbf{K}_i') \rangle^*, \tag{14}$$

and an incoherent component,

$$C_i = C - C_c = \langle T(\mathbf{K}, \mathbf{K}_i)T^*(\mathbf{K}', \mathbf{K}_i') \rangle - \langle T(\mathbf{K}, \mathbf{K}_i) \rangle \langle T(\mathbf{K}', \mathbf{K}_i') \rangle^*. \tag{15}$$

The second moment of the upgoing spectrum, Ψ^+ can also be split into coherent and incoherent contributions, $\langle |\Psi_c^+(\mathbf{K})|^2 \rangle$ and $\langle |\Psi_i^+(\mathbf{K})|^2 \rangle$, where

$$\langle |\Psi^+(\mathbf{K})|^2 \rangle = \langle |\Psi_c^+(\mathbf{K})|^2 \rangle + \langle |\Psi_i^+(\mathbf{K})|^2 \rangle. \tag{16}$$

Some simplifications can be made if the rough interface is wide-sense stationary. Under this assumption, C_i is subject to the following property (Jackson and Richardson, 2007; Voronovich, 1999; Zipfel and DeSanto, 1972):

$$C_i(\mathbf{K}, \mathbf{K}', \mathbf{K}_i, \mathbf{K}_i') = \tilde{C}_i(\mathbf{K}, \mathbf{K}_i, \mathbf{K}_i') \times \delta(\mathbf{K} - \mathbf{K}_i - (\mathbf{K}' - \mathbf{K}_i')). \tag{17}$$

The tilde version of C_i allows the number of arguments to be reduced by one. The scattering cross section per unit solid angle per unit area (hereafter referred simply as the “scattering cross section”) is related to \tilde{C}_i through

$$\sigma(\mathbf{K}_s, \mathbf{K}_i) = k_z^2 \tilde{C}_i(\mathbf{K}_s, \mathbf{K}_i, \mathbf{K}_i), \tag{18}$$

where $k_z = \sqrt{k^2 - |\mathbf{K}|^2}$ is the vertical component of the wave vector (in this case the scattered wave vector). The scattering cross section characterizes the incoherent intensity scattered

into different wavenumber components, or angles, compared to the incident intensity, and is dimensionless [Jackson and Richardson (2007), Chap. 2]. The incoherent contribution to the upgoing plane wave spectrum is computed by integrating through Eq. (12) by \mathbf{K}_i' and using the definition of C_i in terms of σ , resulting in

$$\langle |\Psi_i^+|^2 \rangle = k_{sz}^{-2} \iint \sigma(\mathbf{K}, \mathbf{K}_i) D(\mathbf{K}_i) d^2K_i. \tag{19}$$

The coherent second moment of C can be simplified, again using the assumption of wide-sense stationarity, resulting in

$$C_c(\mathbf{K}, \mathbf{K}', \mathbf{K}_i, \mathbf{K}_i') = R_c(\mathbf{K})R_c^*(\mathbf{K}') \times \delta(\mathbf{K} - \mathbf{K}_i)\delta(\mathbf{K}' - \mathbf{K}_i'), \tag{20}$$

where R_c is the coherent reflection coefficient and itself is defined as

$$R_c(\mathbf{K})\delta(\mathbf{K} - \mathbf{K}_i) = \langle T(\mathbf{K}, \mathbf{K}_i) \rangle. \tag{21}$$

With these two delta functions, the coherent contribution of the upgoing plane wave spectrum can be computed as

$$\langle |\Psi_c^+(\mathbf{K})|^2 \rangle = D^-(\mathbf{K})|R_c(\mathbf{K})|^2. \tag{22}$$

The physical interpretation of this result is that the upgoing plane wave spectrum at each wavenumber is proportional to the downgoing wave spectrum multiplied by the coherent power reflection coefficient.

Putting together Eqs. (10), (11), (16), (19), and (22), the total passive intensity reflection coefficient for an inhomogeneous seafloor can be calculated as

$$\langle |R^P(\mathbf{K})|^2 \rangle = |R_c(\mathbf{K})|^2 + |R_{iw}(\mathbf{K}, D^-(\mathbf{K}))|^2, \tag{23}$$

where the first term is the magnitude squared coherent reflection coefficient and has been defined in Eq. (21). The second term is the weighted incoherent reflection coefficient, defined by

$$|R_{iw}(\mathbf{K}, D^-(\mathbf{K}))|^2 = \frac{1}{D^-(\mathbf{K})k_z^2} \iint \sigma(\mathbf{K}, \mathbf{K}_i) D^-(\mathbf{K}_i) d^2K_i, \tag{24}$$

where the downgoing plane wave intensity, $D^-(K)$ is used as a weighting function. Equations (21), (23), and (24) constitute the main results of this work.

The quantity R_{iw} is similar to the incoherent reflection coefficient, R_i , which has been previously discussed in the literature, e.g., Appendix L of Jackson and Richardson (2007). These two quantities are equal if D^- is a constant function of angle and wavenumber. Since the scattering cross section and coherent reflection coefficient are both dimensionless, Eqs. (23) and (24) are readily verified to be dimensionally consistent.

These wavenumber integrals have domains of $\pm\infty$ for both K_{ix} and K_{iy} . When the horizontal wavenumber magnitude

is greater than k , then the incident waves become evanescent. If these evanescent components are neglected, then the domain of integration can be restricted to $|\mathbf{K}_i| < k$, and the integration can be converted to real angle, instead of wave-number [see, e.g., Holland *et al.* (2012)]. Making this substitution and restricting the domain of integration results in

$$\langle |R_{iw}(\theta)|^2 \rangle = (D^-(\theta) \sin \theta)^{-1} \times \iint \sigma(\theta, \theta_i, \phi_i) D^-(\theta_i) \cos \theta_i d\theta_i d\phi_i. \quad (25)$$

The scattering cross section is, in general, a function of both the incident azimuthal angle, ϕ_i , and the scattered azimuthal angle, ϕ_s . However, for isotropic roughness, σ can only depend on $\phi_s - \phi_i$, and either one may be used alone. The angle θ is the grazing angle at which the array is steered to estimate the reflection coefficient.

Equations (23) and (25) have a simple interpretation. The total scattered energy is due to the sum of coherent and incoherent components. The coherent component is reduced compared to the flat-interface component due to scattering out of the specular direction. In the second term in Eq. (23), incoming waves from all directions are scattered into the wave vector with horizontal component \mathbf{K} , and angle θ . Their relative contribution to the incoherent field in that angle is set by both the incident plane wave power spectrum, D^- , and the bistatic scattering cross section σ .

This process of loss of coherent intensity is graphically illustrated in Fig. 1(a). There, an incoming plane wave is shown by a red arrow with a pointed tip and rounded end. Outgoing scattered incoherent waves are shown by green arrows. A vertical line array is shown in gray and is steered in the specular angle of the incoming plane wave. A black dashed arrow shows the flat interface reflected wave, whereas the yellow dotted line shows the coherent component in the presence of roughness. Note that some incoherent energy is also scattered into the specular direction. The lengths of the arrows are meant to show the relative intensity of the acoustic waves propagating in various directions, but their lengths are not drawn to scale.

In Fig. 1(b), the contributions to the incoherent component are graphically illustrated. If the incident power spectrum is assumed to be constant with angle (the omnidirectional case), then the relative contributions are determined only by σ and k_z . The lengths of the incoming red arrows with rounded ends are meant to show the relative contributions of each incoming plane wave component to the angle, θ , sensed by the vertical line array, shown in gray. The incoherent contribution is shown as a purple outgoing wave that has the same direction as the black dashed line in Fig. 1(a).

The degree of incoherent and coherent scattering depends strongly on the ratio h/λ . As h increases compared with λ , the coherent component generally decreases, and the incoherent component increases. In some cases, such as layered seafloors, the coherent contribution increases with increasing h/λ due to the disruption to the near-perfect cancellation that can sometimes occur with layering. The coherent

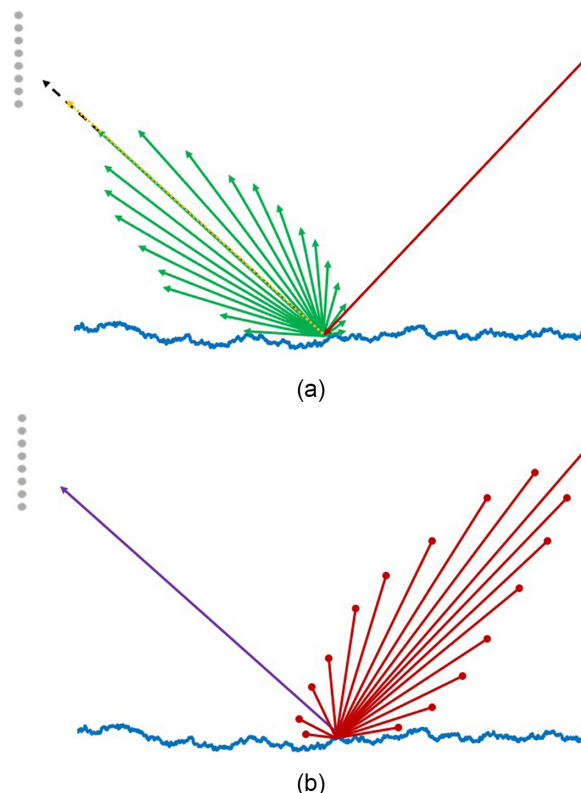


FIG. 1. (Color online) Diagram representing the two contributions to the passive intensity reflection coefficient. In (a) the red arrow shows a single incident plane wave, whose intensity reflection from a flat interface is denoted by a black dashed line. In the presence of roughness, intensity is scattered into non-specular directions, represented by the green arrows. The reduced coherent intensity, $|R_c|^2$, due to scattering is represented by the dotted yellow line. In (b) the incoherent contributions to a single plane wave direction measured by the array is shown by a purple line. The red lines with dots at the end represent the contributions to the incoherent component from other angles. The arrow length represents the contribution to the intensity from that particular direction. The directionality of the incident noise field is not shown in this diagram.

reflection coefficient depends only on the rms roughness, h , and depends on the outer scale only through the dependence of h on K_0 [see Jackson and Olson (2020) and Olson and Jackson (2020) for further discussion and details]. The incoherent component may depend strongly on the outer scale, since the scattering cross section is narrow near the specular direction for K_0 small compared to k and broadens as K_0 increases. Simple formulae for the coherent and incoherent component are not available at present but could be derived using approximations to some of the scattering models used here. Care must be taken when employing approximations because energy conservation must be upheld here. Additionally, traditional simplifications for layered seafloors, such as the Eckart factor have recently been shown to be inaccurate Jackson and Olson (2020). The relative importance of these two terms is explored in Sec. IV.

Some considerations for using a model to compute the coherent and incoherent components of Eq. (23) must be stated. Since integration over all incident and scattered angles is performed in that integral, any model used for the scattering cross section should be accurate over all angles.

The Kirchhoff approximation [Jackson and Richardson (2007), Chap. 13], is considered to be accurate only near the specular direction (Thorsos, 1988, 1990). Perturbation theory is typically considered to be accurate away from the specular direction, but in some circumstances may be accurate over the entire angular range (Thorsos *et al.*, 2000) if the outer scale of the rough interface is comparable to the acoustic wavelength. The small slope approximation is considered to be accurate over the entire angular range, but over a wider set of roughness parameters than perturbation theory [Jackson and Richardson (2007), Chap. 13]. Due to the integrals over angle required for the weighted incoherent reflection coefficient, the small-slope approximation is preferred over the other models in this work.

The form of the main result for Eq. (23) has some similarity to the modelled effect of noncoherent noise on passive reflection measurements. Quijano *et al.* (2012) modeled the effect of noncoherent ambient noise (i.e., noise that is not useful for environmental inference, such as flow noise or thermal noise) as the ratio of the sum of two terms—the upward (or downward) propagating field from coherent noise sources and a signal to noise dependent term. This functional form of the effect of noncoherent noise is quite similar to the main result here. In fact, when ambient noise produced at the surface is incoherently scattered by the seafloor, it becomes a source of non-coherent noise, but with a different angular dependence. In Quijano *et al.* (2012), the SNR per frequency bin was estimated, and it is possible that a fraction of the energy of the non-coherent noise field in that experiment was due to seabed scattering, since all seafloors are rough to some degree. Although this aspect is not explored here, an interesting area for future work to disentangle noncoherent ambient sound due to incoherent seabed scattering and other sources. The precise characteristics of the array (e.g., spacing, length) and processing techniques would need to be taken into account.

IV. NUMERICAL EXAMPLES

In this section, several numerical results are presented using a halfspace model, and a layered seafloor. The halfspace small slope approximation (Gragg *et al.*, 2001), and the recently developed small slope approximation for layered media (Jackson and Olson, 2020) are used for the coherent reflection coefficient and scattering cross section in their respective cases. First, separate curves of the flat interface, coherent, incoherent, and total reflection coefficient are presented—all assuming an omnidirectional ambient noise field. These plots serve to show the basic contributions of each term to the total, and how the total may differ from the flat interface case. Next, the effect of a directional spectrum is examined, using measured noise directionality data at about 2.5 kHz from (Clark, 2007). In all cases the roughness parameters are varied between very slightly rough ($kh = 0.05$), and very rough ($kh = 0.5$). The rms heights of these limiting cases are 1.31 and 13.1 cm, respectively.

For reference, the rms height in historical seafloor roughness measurements reported in Table VI.1 of Jackson and Richardson (2007) have an upper limit of 4.10 cm for an area with shell hash, and an average value of 0.77 cm. However, all of these measurements were one-dimensional, and over a length of approximately 1 m. Surfaces with power-law roughness have mean square values that increase as the measurement length or area is increased, so these reports of h are likely an underestimate, compared with the scales that ambient noise sources interact with the seabed. If these scales are 10 or 100 times the size of the roughness measurement system used for the historical measurements, then the average value of the rms roughness could potentially be over 30 cm. Therefore, the upper limit here of 13.1 cm for h is relatively modest for passive estimates of the seafloor reflection coefficient.

The specific parameters of the von Kármán spectrum are given in Table I. Only the spectral strength is varied to change the non-dimensional rms roughness, kh . All simulations in this section are performed at 2473 Hz, so that the directional noise spectrum published in Clark (2007) can be used. A water sound speed of 1500 m/s was used. The outer-scale was set to $L_0 = 5/k$, and the spectral exponent was set to $\gamma_2 = 3$, so that the fast approximation of the Kirchhoff integral developed in Olson (2021) could be used. The spectral strength varied in order to set kh to the values [0.05, 0.1, 0.3, 0.5]. These roughness parameters were used in both the halfspace and layered simulations.

A. Halfspace example

For the halfspace, a medium with the sound speed ratio, density ratio, and attenuation parameters in the rightmost column of Table II was used. These parameters are close to a medium sand and support a critical angle. The rough interface parameters are specified in Table I. For the halfspace example, the coherent reflection coefficient and scattering cross section are calculated according to the lowest-order halfspace small-slope approximation, expressions for which can be found in Chap. 13 of Jackson and Richardson (2007). The coherent reflection coefficient is the same as under the Kirchhoff approximation, and is the Eckart factor from Eq. (1). In the incoherent reflection coefficient, the small slope approximation requires calculation of the Kirchhoff integral, and the functional Taylor series developed in (Olson, 2021) is used here.

First, the flat interface reflection coefficient is compared to the coherent, incoherent and total (coherent plus incoherent)

TABLE I. Roughness parameters used in the numerical examples.

Parameter	Symbol	$kh = 0.05$	$kh = 0.1$	$kh = 0.3$	$kh = 0.5$
Spectral strength	$w_2 [m^{4-\gamma_2}]$	7.68×10^{-6}	3.08×10^{-5}	2.77×10^{-4}	7.68×10^{-4}
Spectral exponent	$\gamma_2 [—]$	3	3	3	3
Inv. outer scale	$K_0 [m^{-1}]$	2.08	2.08	2.08	2.08

TABLE II. Geoacoustic properties for each of the numerical examples. The rightmost column contains parameters for the single interface example (halfspace), and the second and third from the right columns contain parameters for the single layer example.

Parameter	Symbol	Layer	Basement	Halfspace
Sound speed ratio	ν [m/s]	1.05	1.80	1.17
Density ratio	a_ρ [kg/m ³]	1.8	2.5	1.8
Attenuation	α [dB/m/kHz]	0.02	0.01	0.02
Thickness	d [m]	0.81	—	—

reflection coefficients from the model in Fig. 2. All reflection coefficients are plotted as the magnitude square, which is also the intensity reflection coefficient. In this figure, an omnidirectional incident noise spectrum is used, so that the effect of the scattering cross section and plane wave coherent reflection coefficient can be examined alone. In each subfigure, a different set of roughness parameters is used, specified by kh . Overall, the coherent reflection coefficient is uniformly lower than the flat interface coefficient, as it must be in the Eckart model (Eckart, 1953). As kh is increased, the coherent reflection coefficient decreases, and the incoherent contribution increases. For small values of kh (0.05 and 0.01), the incoherent component is essentially zero, and the total and flat interface coefficients are essentially equal. For a moderate value of $kh=0.3$, the incoherent contribution is small, but non-negligible. In this case, the total reflection coefficient is still approximately equal to the flat-interface coefficient. For the largest roughness case, the total and flat interfaces quantities are still close. However, the total reflection coefficient is slightly lower than the flat interface case at steep angles, and greater at very shallow angles (less than about 20°).

Next, the bottom loss is compared between the total omnidirectional, total directional, and flat interface reflection coefficients. Bottom loss, BL , is defined as

$$BL = -20 \log_{10}|R|, \tag{26}$$

where R is any of the reflection coefficients discussed in this work. The downgoing noise spectrum was taken from Clark (2007), and is plotted in Fig. 3. Although the specific roughness and geoacoustic characteristics of the seafloor, as well as the sound speed profile and surface characteristics determine the ambient sound directionality pattern, this measurement from the literature is used here for illustrative purposes. To perform a real geoacoustic inversion using ambient noise in the presence of a rough seafloor, the actual down-going spectrum would be available from the vertical array.

For the purposes of this paper, the most relevant feature of the directionality pattern is a region of very low intensity near horizontal angles which is sometimes present in ocean ambient sound measurements (Harrison, 2018; Rouseff and Tang, 2006). This feature causes the steep angle portion of the contributions in Eq. (24) to the incoherent reflection coefficient to be highly weighted, even if the scattering cross section is sharply peaked near the specular direction and the beam angle θ is small. This region of low intensity is not always present. The directionality in Fig. 3 also suggests a layered seafloor, since peaks and nulls are visible in both the downgoing and upgoing portions. However, in the downgoing plane wave spectrum, the oscillations due to seafloor interference are very small compared to the intensity difference between steep and shallow angles.

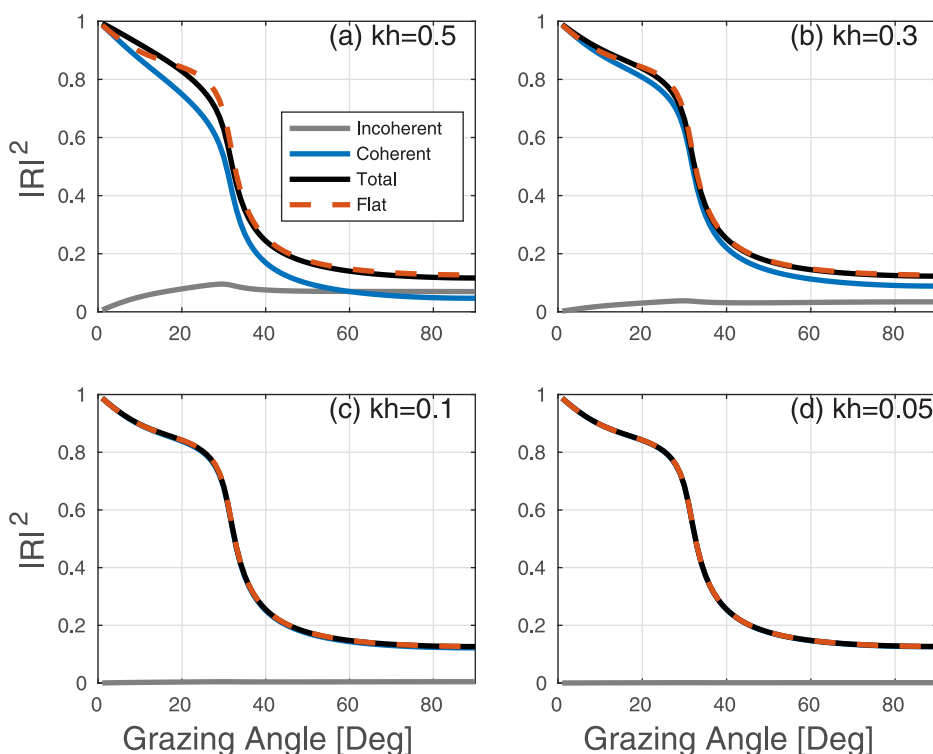


FIG. 2. (Color online) Coherent, incoherent, and total contributions to the intensity reflection coefficient for a halfspace compared with the flat-interface case. Various roughness parameters are plotted, and an omnidirectional noise field is used as the incident field.

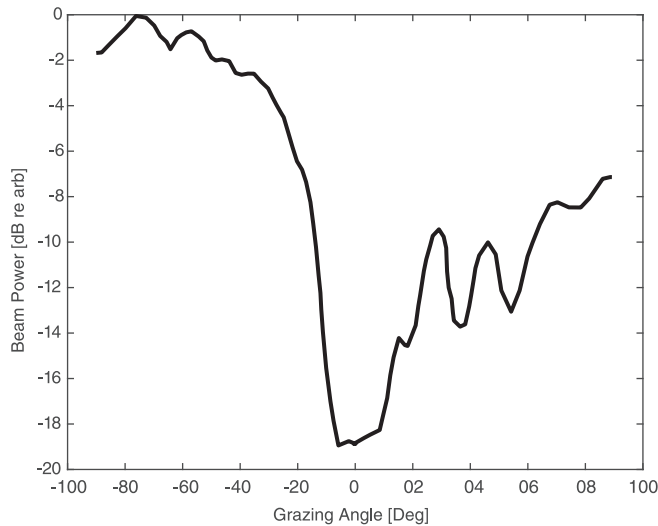


FIG. 3. Noise directivity used for numerical examples employing a directional noise incident field, taken from Clark (2007). Negative angles indicate downgoing energy, and positive angles are upgoing. As this is a measurement, it does not represent the true ambient noise directivity pattern but includes the effect of array response.

Using this measurement for $D^-(\theta)$ in the incoherent weighted reflection coefficient, Eq. (24), results for total bottom loss are plotted in Fig. 4. Here, the flat interface, omnidirectional total, and directionally weighted total reflection coefficients are compared, again for the halfspace case. The $kh = 0.05$ case was neglected here since the BL curves were essentially the same as the $kh = 0.1$ case. The three curves diverge slightly as kh is increased. Also, BL is slightly negative for the directional source and large kh values. For a single plane wave incident field, negative bottom loss is non-physical, but arises in this case due to the nonuniform intensity distribution of the incident plane wave spectrum.

B. Single layer example

The second numerical example consists of a single layer with a halfspace below. The water-sediment interface is rough, and the layer-basement interface is flat. The parameters of the layer and basement are given in Table II, columns 3 and 4. The layer sound speed is slightly higher than the water sound speed, and the basement sound speed is significantly higher than both. The high contrast between the layer and the basement leads to significant modal structure in the flat interface plane wave reflection coefficient. The same roughness parameters are used, as for the halfspace case. The small slope approximation for layered, fluid seafloors (Jackson and Olson, 2020) was used as a model for the coherent reflection coefficient and scattering cross section, and the series approximation of Olson (2021) was used to evaluate the large number of evaluations of the Kirchhoff integral required by small slope. This model was shown to be accurate for 1D roughness for kh up to 0.66 in (Olson and Jackson, 2020), which exceeds the largest value used in this work. Formulae for the flat interface reflection coefficient for layered fluid media can be found in standard texts (Brekhovskikh and Godin, 1990; Jensen et al., 2011).

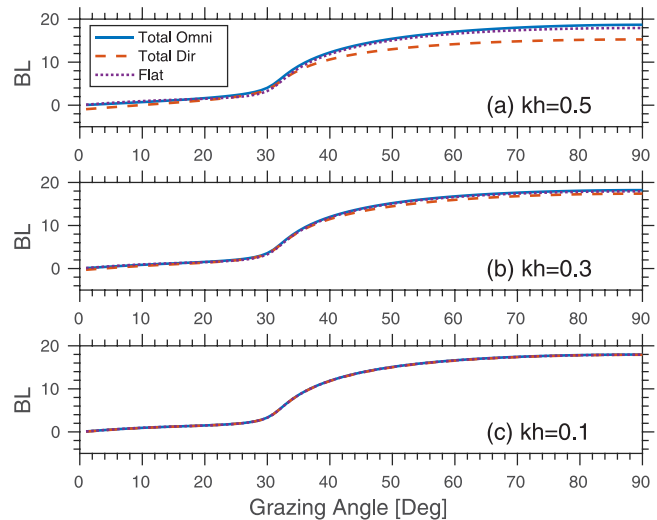


FIG. 4. (Color online) Comparison of bottom loss for a halfspace computed using the omnidirectional incident field, versus a directional noise field taken from Clark (2007). The flat interface bottom loss is also plotted.

As before, the flat interface, coherent, incoherent, and total reflection coefficients are compared, and plotted in Fig. 5. Similar to the halfspace case, the two smallest roughness cases have virtually identical flat, coherent, and total reflection coefficients, while the incoherent contribution is virtually zero. For $kh = 0.3$ and 0.5 , the incoherent contribution becomes more important. For the $kh = 0.3$ case, the flat interface and total reflection coefficients are very close for the majority of angular domain. Above about 70° grazing angle, the flat interface coefficient is very small, and a null occurs at about 80° grazing angle. Interestingly, the coherent component is larger in magnitude than the flat interface coefficient at this specific angle, especially in the $kh = 0.5$ case. The inclusion of the incoherent coefficient, which is positive definite, only further increases the reflection coefficient and widens the disparity between the total and flat interface coefficients. In Jackson and Olson (2020) and Olson and Jackson (2020), this increase in the coherent reflection coefficient near a minimum was interpreted to be the result of a disruption to the perfectly destructive interference due to the presence of roughness. The total reflection coefficient is much different than the flat interface coefficient at these high angles and may impact geoaoustic inversion if a flat interface model is assumed.

Including the effect of a directional noise field is presented next, using the measurement from (Clark, 2007) in Fig. 3. As before, the omnidirectional total, directionally weighted total, and flat interface bottom loss are presented in Fig. 6. The most notable feature in this figure is the pronounced peak in BL at 80° . The log-transformation used in calculating BL enhances the difference between the flat and total BL , especially when the magnitude of the reflection coefficient is small. Even for the smallest roughness case, there is a difference of about 10–20 dB between the flat and both total BL curves. At other angles, the difference between all three curves is smaller. For the two largest roughness

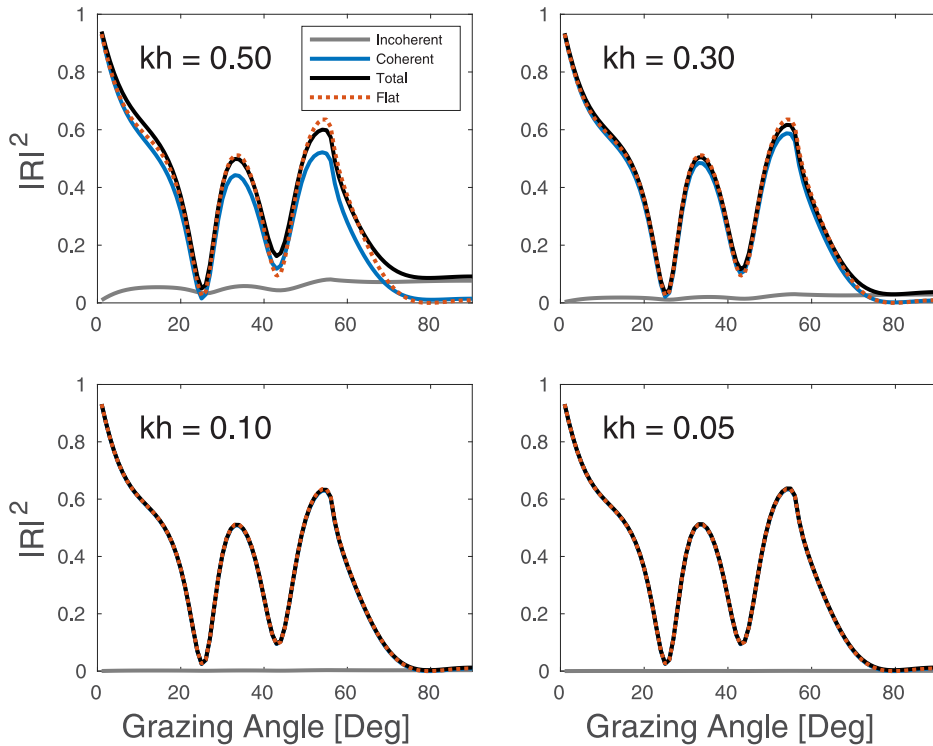


FIG. 5. (Color online) For the layered seafloor, the coherent, incoherent, total, and flat-interface reflection coefficients are compared. Four different roughness parameters are used, and an omnidirectional incident noise field was assumed.

cases, the directional total BL dips slightly below 0dB at very small angles, as for the halfspace case. If used with inverse methods that employ a flat interface model [such as Quijano *et al.* (2012)], these differences between the total and flat reflection coefficients may result in an inaccurate estimate of geoacoustic parameters if significant roughness is present.

V. SIMULATED INVERSIONS

In Sec. IV, it was shown that the presence of roughness has a noticeable impact on the measured passive reflection coefficient. However, it is important to understand the effects of roughness on inverse methods. First, a flat interface model is fit to simulated data in order to simulate the effect of ignoring roughness (an assumption in all previous literature on inversions using ambient sound and most previous literature using active sources). Second, an inversion for both roughness and geoacoustic properties is performed to demonstrate the feasibility of this model for future inversions using ambient sound measurements collected in the field.

A. Effect of roughness on geoacoustic inversion errors

Given the differences observed between the total reflection coefficient and the flat interface coefficient, it is important to inquire about the effect of roughness on geoacoustic inversion. To that end, in this subsection, the total reflection coefficient (both omnidirectional, and directional) for the layered case is used as synthetic data and a flat interface model is fit to bottom loss. The synthetic data is unrealistic for an experimental situation, in that no uncertainty (due to a

finite number of averages snapshots) or noncoherent noise (such as flow or thermal noise) is present. However, this analysis illustrates the effect that scattering may have on passive geoacoustic inversion when inappropriate

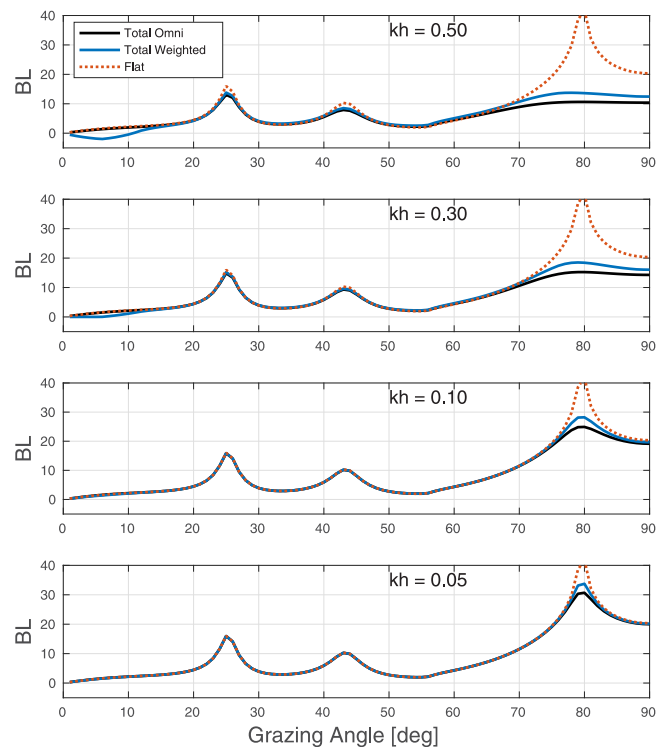


FIG. 6. (Color online) Comparison of bottom loss for a layered seafloor computed using the omnidirectional incident field, versus a directional noise field taken from Clark (2007). The flat interface bottom loss is also plotted.

assumptions are made. For ambient noise inverse methods, many frequencies are used, which reduces the ambiguity and increases the information content compared to a single frequency. For this reason, this simulated flat interface inversion is performed at two frequencies, namely, 2473 and 3000 Hz.

The flat interface model parameters are estimated using a bounded version of the Nelder-Mead downhill simplex optimization (Nelder and Mead, 1965). The downhill simplex algorithm is an unbounded method (i.e., no constraints on the parameters), but a constrained version can be implemented by using a coordinate transformation to a domain where the objective function is periodic. After the optimization is finished, the parameters are mapped back to the original parameter space. Each parameter ψ_i is constrained to an interval $[a_i, b_i]$, where a_i is the lower bound for the parameter index i and b_i is the corresponding upper bound. The constraints are implemented by transforming each bounded variable, ψ_i to u_i , which are related by the following two equations (D’Errico, 2022):

$$u_i = \sin^{-1} \left(\frac{2(\psi_i - a_i)}{b_i - a_i} - 1 \right), \tag{27}$$

$$\psi_i = \frac{\sin(u_i) + 1}{2} (b_i - a_i) + a_i. \tag{28}$$

The lower and upper bounds for each of the geoacoustic parameters and layer thickness are given in the first four rows of Table III.

The cost function was the sum of squares residual between the total (i.e., simulated data), and flat-interface (i.e., model) bottom loss, which is commonly used in other geoacoustic inversion methods (Dettmer and Dosso, 2012; Quijano *et al.*, 2012). Since this method is subject to becoming stuck in local minima, many starting parameters are used, about 6000. The starting locations were randomly drawn from a uniform distribution with support determined by the bounds given in Table III. Only angles between 10° and 90° grazing angle were used in the fit, given that the flat interface model cannot fit negative *BL*. The angular domain was sampled at 1° increments.

A comparison of the total *BL* (both omni and directionally weighted) to the flat interface fit is shown in Fig. 7, at both frequencies (2473 Hz in the left column and 3000 Hz in the right column). Since the *kh* values are different for each frequency, the specific values have been displayed in the subplots. The directional and omnidirectional input data (total reflection coefficients are shown in solid lines of different colors, and the model fits are shown in dashed lines of different colors—specified in the figure legend. Overall, a good fit is obtained using a flat interface model, apart from several isolated locations. Near the peaks in bottom loss (grazing angles of 25° and 45°) the flat interface model does not provide a good fit. In the smaller roughness cases, virtually perfect agreement is found between the best fit flat interface model, and the total omnidirectional reflection coefficient. For the directive total reflection coefficient, the

flat interface model does not provide as good of a fit for the two smallest roughness cases.

Even if a good fit can be found, the best fit parameters may not be the same as the inputs. The error compared to the input is shown in Fig. 8 for each parameter. In each sub-figure, the percent error of a given parameter of the flat interface model is shown as a function of *kh* on the horizontal axis. For all parameters except for the layer thickness, four parameters are plotted—two for the layer and half-space, each estimated from the omnidirectional and directional datasets. Also, shown is a fit of the flat interface model to a flat interface simulated data, these results are listed as *kh* = 0. Note that only omnidirectional results are shown for *kh* = 0, since there is no incoherent contribution, regardless of the noise directivity. Essentially perfect fit is found to the flat interface model for all parameters.

In general, the error increases with *kh*. The trends for the parameters are not monotonic, but the absolute value of error typically increases with increasing *kh*. The estimated layer thickness and layer sound speed are quite consistent with the inputs, with a maximum error of only a few percent. The basement sound speed, on the other hand has a large error for large *kh*. Since the layer properties together with the acoustic frequency determine the locations of maxima and minima of the interference pattern in the reflection coefficient, it is sensible that the layer thickness and sound speed are not too much altered by the presence of scattering. Although the height of the peaks and troughs in *BL* (see Fig. 7) are altered in the presence of roughness, their locations in angle are preserved.

Density, on the other hand has large errors compared to the input geoacoustic parameters, even for moderate values of the rms roughness. This error exists because the amplitudes of the reflection coefficient fringes are affected by density, but not the location of the interference fringes.¹ Attenuation estimates also have large errors. Like with density, the strength of the peaks and nulls are highly dependent on the attenuation coefficient of the layer and basement, even more so than density, since a strongly attenuating layer can suppress interference in the layer. That is, with significant attenuation, perfect cancellation becomes impossible. Since the presence of roughness can cause a reduction in the coherent reflection coefficient and decrease the high *BL* peaks due to incoherent scattering, an altered attenuation parameter may provide a good fit, as evidenced by the good match in Fig. 7. Since the high *BL* regions are the most distorted in the total reflection coefficient, it is reasonable that the inversion converged on significantly different attenuation parameters. In the geoacoustic literature, attenuation for all layers, as well as basement properties in general has been demonstrated to be difficult to estimate in both experiments (Belcourt *et al.*, 2020; Holland *et al.*, 2012) and simulations (Dettmer *et al.*, 2007, 2009, 2010). Use of an inappropriate model may be a contributor to high uncertainties in experimental data, but a controlled experiment with ground truth is needed to make a more definitive conclusion.

TABLE III. Parameter bounds for flat interface inverse model.

Symbol	[Unit]	Lower	Upper
ν	[—]	0.9	2.5
a_p	[—]	1.4	3
α	[dB/m/kHz]	0.001	1
d	[m]	0.1	3
h	[m]	10^{-3}	10^{-1}
K_0	[m^{-1}]	10^{-3}	10^1

B. Joint roughness and geoacoustic inversion

In Sec. V A it was demonstrated that using an inappropriate model can lead to errors in modestly rough seafloors. In this section, roughness parameters have been included in the inversion to demonstrate that this model has potential for inversion of at-sea field data. Both simulated data and the forward model for the inversion are computed using the model developed in Sec. III. Again, two frequencies are used in the inversion, 2473 and 3000 Hz, but only an omnidirectional incident noise field is used, due to computational

complexity of the model. The bounded downhill simplex with the same parameter bounds was used here as well. Bounds for geoacoustic parameters are listed in the first four rows of Table III (and are the same as Sec. V A), and the last two rows represent the bounds on the roughness parameters. Since h and K_0 can vary over several orders of magnitude, the search space is performed on the base-ten logarithm of these parameters and converted back after the search is finished. The inversions were performed for the four different roughness parameters found in Table I, as before.

The total number of parameters is 9, and the forward model is much more computationally expensive than for the flat interface model. Therefore, only 136 randomly chosen starting locations were used, and a tolerance on the parameters was set to 10^{-2} and used as the termination criterion. Parallel processing was used to perform each of these searches independently. After the search was completed, the run with the smallest error in bottom loss was used as the starting location in a refined downhill simplex run where the tolerance criterion for each parameter was reduced to 10^{-4} . The initial inversions

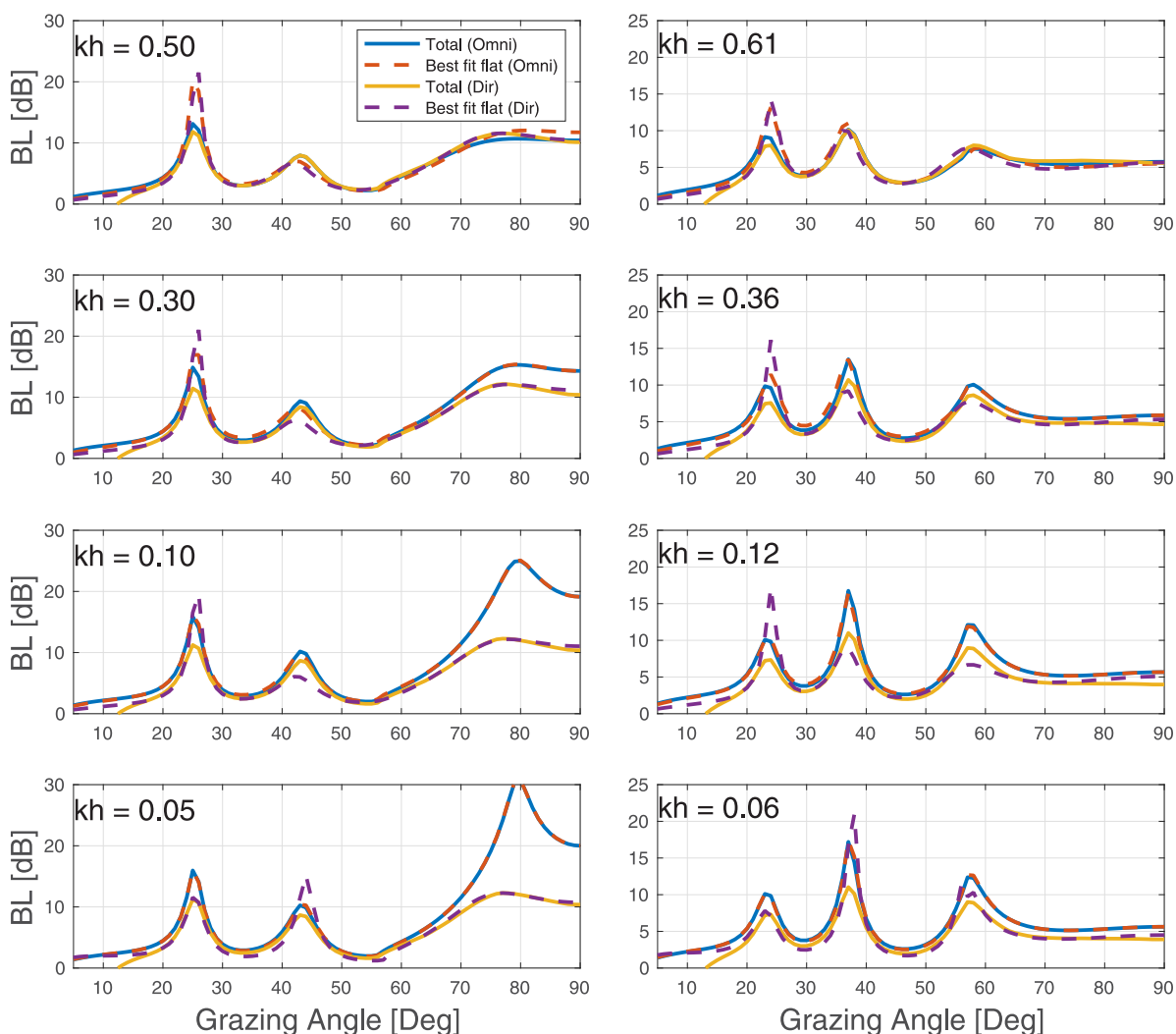


FIG. 7. (Color online) Comparison of total bottom loss compared to an inversion using a flat interface. Both omnidirectional noise and directional noise from Clark (2007) are shown. Two frequencies are shown: 2473 Hz in the left column and 3000 Hz in the right column.

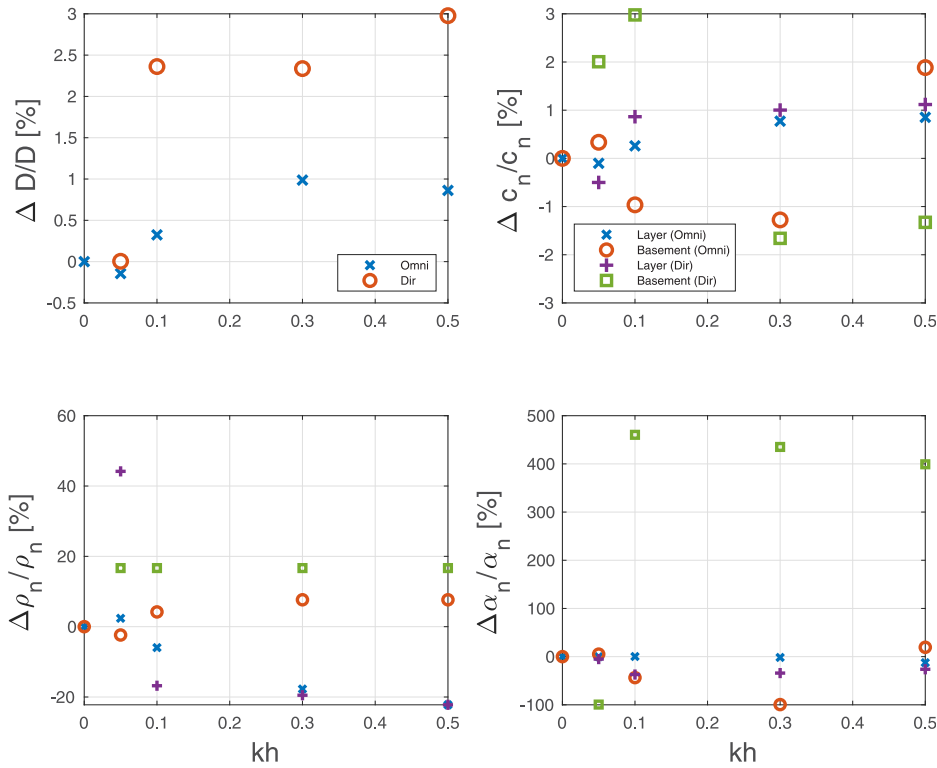


FIG. 8. (Color online) Best fit parameter mis-fit compared to the true parameters. Parameters for both omnidirectional and directional noise spectra are shown, and for both the layer and basement. In general, as the roughness increases, the inverted parameters are increasingly biased, compared to the true parameters. Note that no directional results are shown for $kh=0$, since there is no incoherent contribution in that case.

are referred to as the “coarse” estimates, and the latter as the “refined.”

A summary of the terminal objective function values is given in Fig. 9. The terminal bottom loss error (mean square difference) is plotted against the maximum absolute error in parameter for each inversion run. Both coarse and refined estimates are shown. This figure gives an idea of how sensitive the incoherent bottom loss is to the parameters, which informs whether it is a good metric. The coarse estimates (with tolerance of 10^{-2}) are plotted as circles, the best coarse fit is marked with an X, and the triangles represent the refined estimate. Both axes are log-scaled. Apart from some fluctuations, the error in BL is highly correlated to the error in the parameters, indicating that the joint roughness and geoacoustic cost function is sensitive to the parameters. Power law behavior was observed between the two error metrics. Interestingly, the highest kh case has the most linear dependence of all the parameters, and relatively little fluctuation around this trend. The smallest kh case has much more scatter between the BL error and parameter error, indicating that for small values of kh , bottom loss is less sensitive to errors in the parameter than at larger values of kh . This variation in sensitivity with kh makes sense because for small values of kh the BL curve tends to the flat-interface result.

Next, the best fit bottom loss curves for both frequencies is plotted for each value of kh in Fig. 10. On the left column, the results at 2473 Hz are shown and the 3000 Hz results are shown on the right column. Only the largest three values of kh are shown and are different for each frequency. The BL resulting from the coarse inversion are shown in light gray, along with the input data, and refined results in black and

dotted red respectively. Overall, the refined inversions match the input quite well. The coarse results are much more variable, with some of them matching the shape of the input curve well, and some missing the mark by a wide margin. This large degree of variability indicates that the parameter

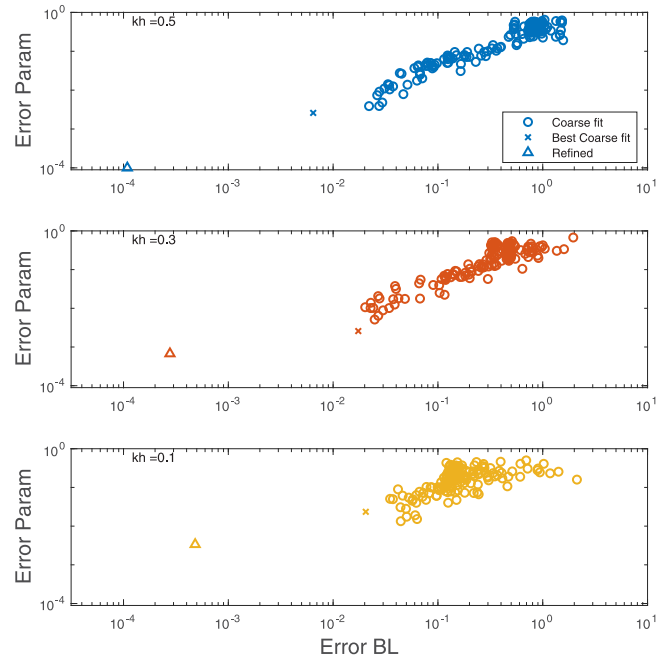


FIG. 9. (Color online) A scatterplot of the error in bottom loss (the cost function used for the inversion) versus the maximum absolute error over all 9 parameters. Each circle represents the termination of the coarse inversion with an X marking the best coarse fit. The trigangles represent the termination of the refined inversion.

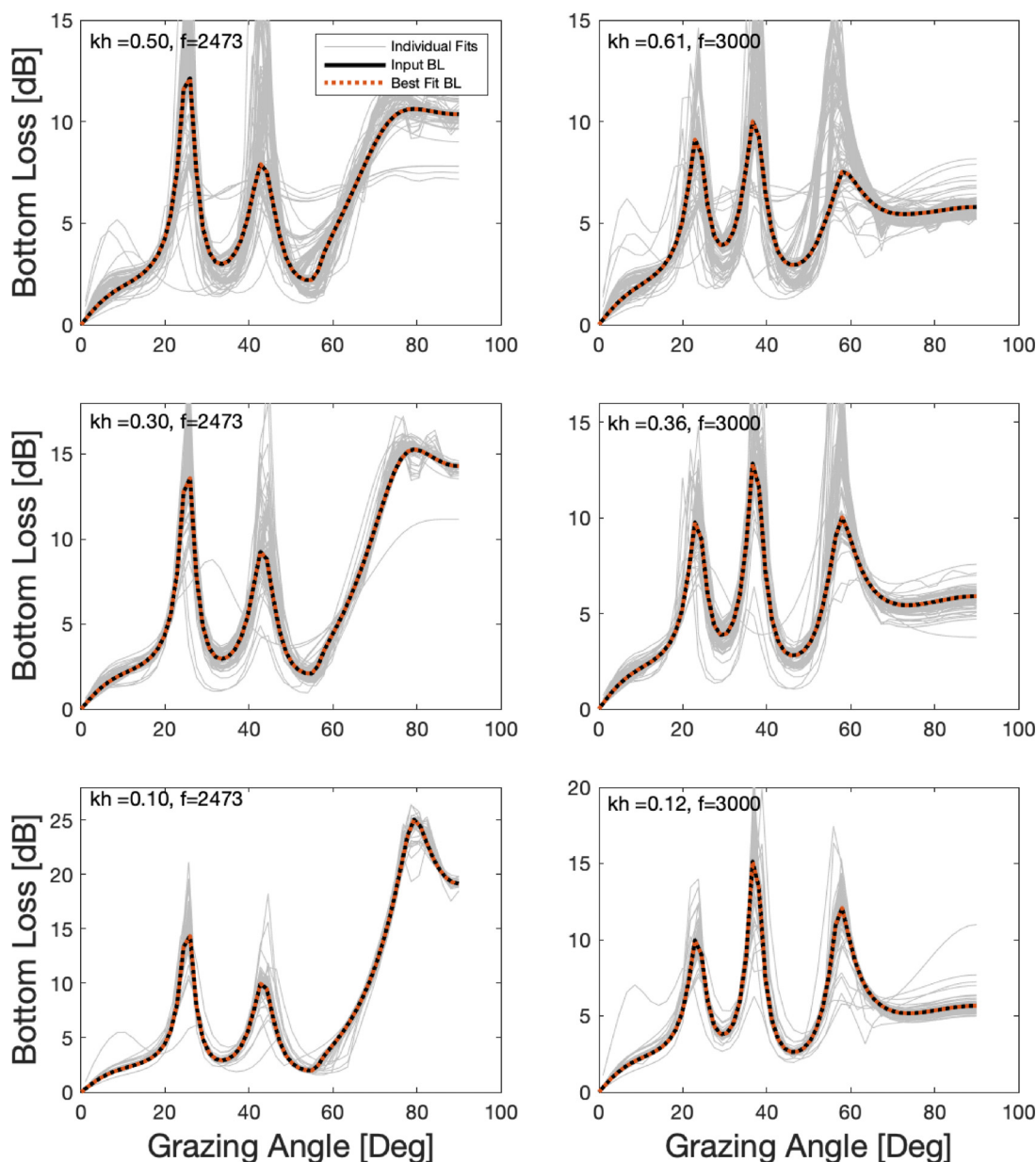


FIG. 10. (Color online) A scatterplot of the error in bottom loss (the cost function used for the inversion) versus the maximum absolute error over all nine parameters. Each point represents the termination of the 136 random start from the coarse inversion, and the results of the refined inversion.

space likely has multiple local minima in the objective function and underscores the necessity for a thorough search of the parameter space (achieved through the random starting locations in this work). Future work using Bayesian estimates of the posterior probability distributions is needed to help elucidate the parameter space interdependencies, and correlations for these inversions.

A summary of the error of the refined estimates is presented in Table IV. For this noise free simulated inversion, the errors are quite low for the majority of the parameters, especially the layer thickness, d , and the sound speed ratios of the layer and basement, ν . Since these two parameters are related to the location of the troughs and peaks in the BL vs angle curve, it makes sense that they have low error. Basement attenuation, α has a higher error, likely because bottom loss is

relatively insensitive to this parameter (as discussed in Sec. VA). The rms roughness, h has a small error, but not as small as the layer thickness or sound speed ratios. The error for the outer scale parameter, K_0 , is one to two orders of magnitude greater than that for h , making it the least resolved parameter in this simulation. The maximum parameter error vs bottom loss error plotted in Fig. 9 is driven primarily by this parameter, since it has the largest error. For $kh = 0.1$ the error in K_0 is about 1% but is about 1/100th the value for $kh = 0.5$. This strong dependence on kh is because the small rms roughness cases are not too different from the flat interface model, as shown in Fig. 5, and the large rms roughness causes a significant departure. Note that the errors in the geoacoustic parameters for all cases are lower than their corresponding error when a flat interface model is used (Fig. 8).

TABLE IV. Parameter errors for refined joint roughness and geoacoustic inversion. Errors are expressed in percent errors relative to the input parameter.

Name	% Err(kh = 0.5)	% Err(kh = 0.3)	% Err(kh = 0.1)
d	1.68e-05	6.01e-04	-2.32e-04
h	-2.20e-03	-3.88e-03	-2.09e-02
K_0	3.15e-02	2.13e-01	1.06e+00
ν (layer)	7.06e-05	1.19e-04	-1.85e-04
ν (basement)	-1.00e-04	8.59e-05	7.46e-03
a_ρ (layer)	-2.69e-03	-5.09e-03	-3.95e-03
a_ρ (basement)	-1.04e-03	1.20e-02	-9.90e-03
α (layer)	1.04e-03	-4.24e-03	-1.72e-03
α (basement)	-6.36e-02	-6.67e-03	-2.13e-01

For the two roughness parameters, the rms height has by far the larger effect on the bottom loss and the outer scale has the smaller effect. This dependence is illustrated graphically in Fig. 11. In this figure, bottom loss for the $kh = 0.5$

parameter set is plotted as a black dashed line, and both h and K_0 are independently varied using logarithmic spacing. For the 2473 Hz case, kh ranges between 0.2 and 0.79 and K_0/k ranges between 0.02 and 2. Both cases produce approximately the same variations in BL, but require much greater variation to produce these changes, two orders of magnitude for K_0 , and a factor of 4 for h (approximately 1/6th of an order of magnitude).

VI. CONCLUSION

In this work, a simple model for the effect of roughness on passive measurements of the total intensity reflection coefficient was derived. The assumptions of this model are an isovelocity sound speed profile, a perfectly diffuse surface noise field, and stationary Gaussian seafloor roughness. Examples were given for a halfspace with a critical angle, and a layered seafloor. It was demonstrated that significant errors in the inverted parameters result when fitting a flat

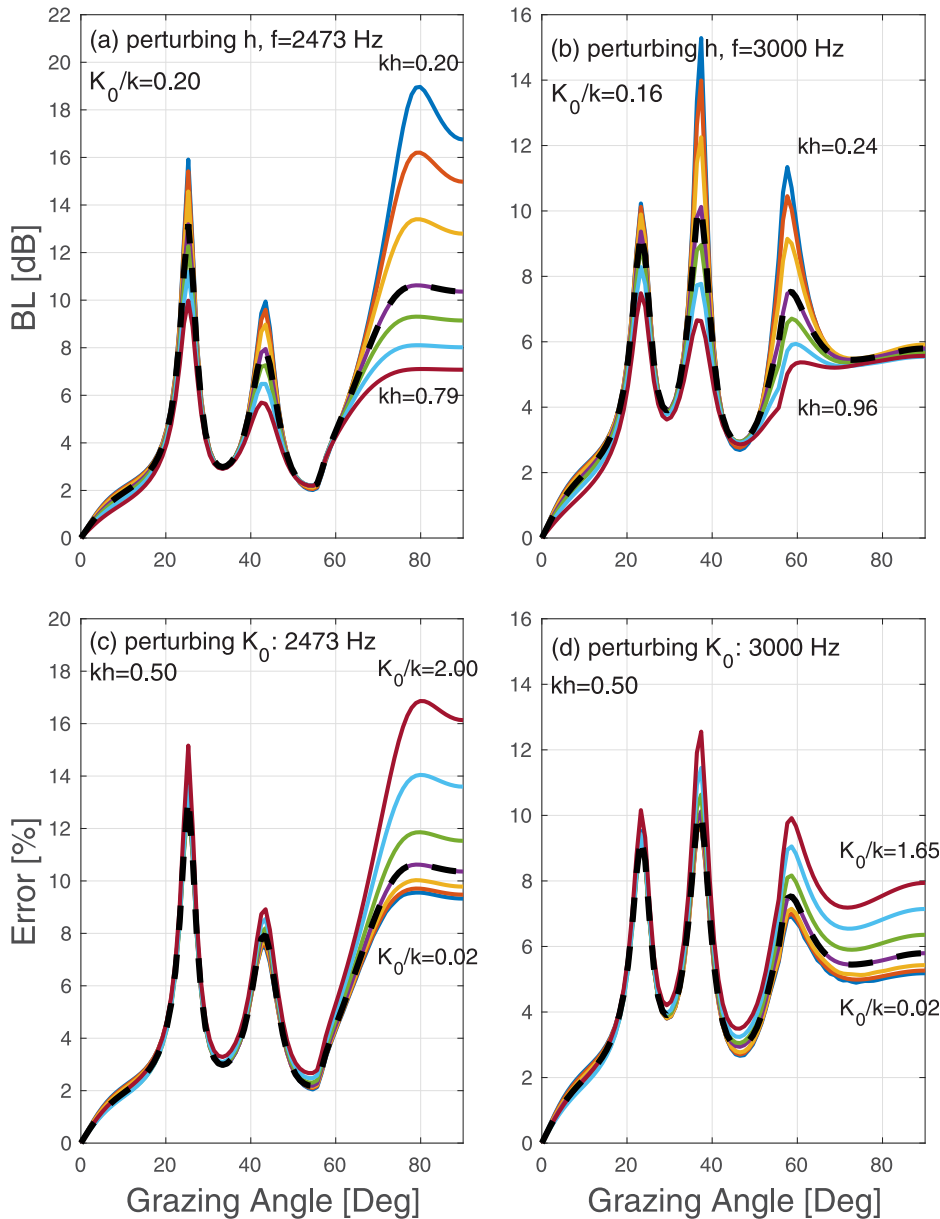


FIG. 11. (Color online) Comparison of the effect of perturbing h and K_0 independently on BL versus grazing angle for the two frequencies used in this section. To obtain the same deviations in the BL curves, much greater variations in K_0 are needed compared to h . In (a) the frequency is 2473 and h is varied. In (b) the frequency is 3000 Hz and h is varied. In (c), the frequency is 2473 and K_0 is varied. In (d) the frequency is 3000 Hz and K_0 is varied.

interface model to data simulated from a rough seafloor. When using the proposed model both as simulated data, and the forward model in a joint roughness and geoacoustic inversion, it was demonstrated that the roughness and geoacoustic parameters can be recovered.

To compare with real measurements, a fruitful area for future work would be to adapt this scattering model to variable sound speed profiles with nonzero attenuation coefficients. Additionally, taking into account the characteristics of a given array should be performed when comparing to any field measurements collected at sea. The simple joint inversion of roughness and geoacoustic parameters gives credence that this model is sensitive to both of the roughness parameter. Another area for future work would be to use Bayesian techniques to examine parameter correlations between roughness and geoacoustic properties. The functional form of the total incoherent reflection coefficient also has some similarity to analytic expressions that account for non-coherent ambient sound. Since scattering by roughness is in fact a source of non-coherent sound (e.g., flow or thermal noise), a study on the relative effects of surface noise scattered by the bottom, and noncoherent sound should be carried out.

ACKNOWLEDGMENTS

The author acknowledges helpful discussions with Dr. Martin Siderius. Funding was provided by the U.S. Office of Naval Research, for which the author is grateful. Any opinions, findings, and conclusions or recommendations expressed in this publication are those of the author and do not necessarily reflect the views of the U.S. Navy.

¹Except for the case of a medium with an angle of intromission, which is not the case here (Kinsler *et al.*, 2000).

- Ballard, M. S., Costley, R. D., Sagers, J. D., Lee, K. M., McNeese, A. R., Hathaway, K. K., Wilson, P. S., and Smith, E. W. (2018). "A comparison between directly measured and inferred wave speeds from an acoustic propagation experiment in Currituck sound," *J. Acoust. Soc. Am.* **143**(1), 237–247.
- Belcourt, J., Holland, C. W., Dosso, S. E., Dettmer, J., and Goff, J. A. (2020). "Depth-dependent geoacoustic inferences with dispersion at the New England Mud Patch via reflection coefficient inversion," *IEEE J. Oceanic Eng.* **45**(1), 69–91.
- Brekhovskikh, L. M., and Godin, O. A. (1990). *Acoustics of Layered Media I: Plane and Quasi-Plane Waves* (Springer, Berlin).
- Brooks, L. A., and Gerstoft, P. (2009). "Green's function approximation from cross-correlations of 20–100hz noise during a tropical storm," *J. Acoust. Soc. Am.* **125**(2), 723–734.
- Brown, S. R., and Scholz, C. H. (1985). "Broad bandwidth study of the topography of natural rough surfaces," *J. Geophys. Res.* **90**(B14), 12575–12582, <https://doi.org/10.1029/JB090iB14p12575>.
- Clark, C. A. (2007). "Vertical directionality of midfrequency surface noise in downward-refracting environments," *IEEE J. Oceanic Eng.* **32**(3), 609–619.
- D'Errico, J. (2022). "fminsearchbnd, fminsearchco," Available at <https://www.mathworks.com/matlabcentral/fileexchange/8277-fminsearchbnd-fminsearchco> (Last viewed 13 September 2022).
- Dettmer, J., and Dosso, S. E. (2012). "Trans-dimensional matched-field geoacoustic inversion with hierarchical error models and interacting Markov chains," *J. Acoust. Soc. Am.* **132**(4), 2239–2250.
- Dettmer, J., Dosso, S. E., and Holland, C. W. (2007). "Full wave-field reflection coefficient inversion," *J. Acoust. Soc. Am.* **122**(6), 3327–3337.
- Dettmer, J., Dosso, S. E., and Holland, C. W. (2009). "Model selection and Bayesian inference for high-resolution seabed reflection inversion," *J. Acoust. Soc. Am.* **125**(2), 706–716.
- Dettmer, J., Dosso, S. E., and Holland, C. W. (2010). "Trans-dimensional geoacoustic inversion," *J. Acoust. Soc. Am.* **128**(6), 3393–3405.
- Eckart, C. (1953). "The scattering of sound from the sea surface," *J. Acoust. Soc. Am.* **25**, 566–570.
- Godin, O. A., Brown, M. G., Zabolot, N. A., Zabolotina, L. Y., and Williams, N. J. (2014). "Passive acoustic measurement of flow velocity in the Straits of Florida," *Geosci. Lett.* **1**(1), 16.
- Gragg, R. F., Wurmser, D., and Gauss, R. C. (2001). "Small-slope scattering from rough elastic ocean floors: General theory and computational algorithm," *J. Acoust. Soc. Am.* **110**(6), 2878–2901.
- Harrison, C. H. (2018). "The ocean noise coherence matrix and its rank," *J. Acoust. Soc. Am.* **143**(3), 1689–1703.
- Harrison, C. H., and Simons, D. G. (2002). "Geoacoustic inversion of ambient noise: A simple method," *J. Acoust. Soc. Am.* **112**(4), 1377–1389.
- Holland, C. W., and Dettmer, J. (2013). "In situ sediment dispersion estimates in the presence of discrete layers and gradients," *J. Acoust. Soc. Am.* **133**(1), 50–61.
- Holland, C. W., Nielsen, P. L., Dettmer, J., and Dosso, S. (2012). "Resolving meso-scale seabed variability using reflection measurements from an autonomous underwater vehicle," *J. Acoust. Soc. Am.* **131**(2), 1066–1078.
- Holland, C. W., Pinson, S., Smith, C. M., Hines, P. C., Olson, D. R., Dosso, S. E., and Dettmer, J. (2017). "Seabed structure inferences from TREX13 reflection measurements," *IEEE J. Oceanic Eng.* **42**(2), 268–288.
- Jackson, D., and Olson, D. R. (2020). "The small-slope approximation for layered, fluid seafloors," *J. Acoust. Soc. Am.* **147**(1), 56–73.
- Jackson, D. R., and Richardson, M. D. (2007). *High-Frequency Seafloor Acoustics* (Springer, New York).
- Jensen, F. B., Kuperman, W. A., Porter, M. B., and Schmidt, H. (2011). *Computational Ocean Acoustics* (Springer, New York).
- Kinsler, L. E., Frey, A. R., Coppens, A. B., and Sanders, J. V. (2000). *Fundamentals of Acoustics*, 4th ed. (Wiley, New York).
- Kuperman, W. A., and Ingenito, F. (1980). "Spatial correlation of surface generated noise in a stratified ocean," *J. Acoust. Soc. Am.* **67**(6), 1988–1996.
- Li, J., Gerstoft, P., Siderius, M., and Fan, J. (2020). "Inversion of head waves in ocean acoustic ambient noise," *J. Acoust. Soc. Am.* **147**(3), 1752–1761.
- Li, J., Siderius, M., Gerstoft, P., Fan, J., and Muzi, L. (2021). "Head-wave correlations in layered seabed: Theory and modeling," *JASA Express Lett.* **1**(9), 096001.
- Muzi, L., Siderius, M., Quijano, J. E., and Dosso, S. E. (2015). "High-resolution bottom-loss estimation using the ambient-noise vertical coherence function," *J. Acoust. Soc. Am.* **137**(1), 481–491.
- Nelder, J. A., and Mead, R. (1965). "A simplex method for function minimization," *Comput. J.* **7**(1), 308–327.
- Olson, D. R. (2021). "A series approximation to the Kirchhoff integral for Gaussian and exponential roughness covariance functions," *J. Acoust. Soc. Am.* **149**(6), 4239–4247.
- Olson, D. R., and Jackson, D. (2020). "Scattering from layered seafloors: Comparisons between theory and integral equations," *J. Acoust. Soc. Am.* **148**(4), 2086–2095.
- Quijano, J. E., Dosso, S. E., Dettmer, J., Zurk, L. M., and Siderius, M. (2013). "Trans-dimensional geoacoustic inversion of wind-driven ambient noise," *J. Acoust. Soc. Am.* **133**(1), EL47–EL53.
- Quijano, J. E., Dosso, S. E., Dettmer, J., Zurk, L. M., Siderius, M., and Harrison, C. H. (2012). "Bayesian geoacoustic inversion using wind-driven ambient noise," *J. Acoust. Soc. Am.* **131**(4), 2658–2667.
- Rouseff, D., and Tang, D. (2006). "Internal wave effects on the ambient noise notch in the East China Sea: Model/data comparison," *J. Acoust. Soc. Am.* **120**(3), 1284–1294.
- Siderius, M., and Gebbie, J. (2019). "Environmental information content of ocean ambient noise," *J. Acoust. Soc. Am.* **146**(3), 1824–1833.
- Siderius, M., Song, H., Gerstoft, P., Hodgkiss, W. S., Hursky, P., and Harrison, C. (2010). "Adaptive passive fathometer processing," *J. Acoust. Soc. Am.* **127**(4), 2193–2200.
- Steininger, G., Dosso, S. E., Holland, C. W., and Dettmer, J. (2014). "Estimating seabed scattering mechanisms via Bayesian model selection," *J. Acoust. Soc. Am.* **136**(4), 1552–1562.

- Steininger, G., Holland, C. W., Dosso, S. E., and Dettmer, J. (2013). "Seabed roughness parameters from joint backscatter and reflection inversion at the Malta Plateau," *J. Acoust. Soc. Am.* **134**(3), 1833–1842.
- Thorsos, E. I. (1988). "The validity of the Kirchhoff approximation for rough surface scattering using a Gaussian roughness spectrum," *J. Acoust. Soc. Am.* **83**, 78–92.
- Thorsos, E. I. (1990). "Acoustic scattering from a 'Pierson-Moskowitz' sea surface," *J. Acoust. Soc. Am.* **88**(1), 335–349.
- Thorsos, E. I., Jackson, D. R., and Williams, K. L. (2000). "Modeling of subcritical penetration into sediments due to interface roughness," *J. Acoust. Soc. Am.* **107**, 263–277.
- Voronovich, A. G. (1999). *Wave Scattering from Rough Surfaces*, 2nd ed. (Springer, Berlin).
- Woolfe, K. F., Lani, S., Sabra, K. G., and Kuperman, W. A. (2015). "Monitoring deep-ocean temperatures using acoustic ambient noise," *Geophys. Res. Lett.* **42**(8), 2878–2884, <https://doi.org/10.1002/2015gl063438>.
- Zhou, Z., Bianco, M., Gerstoft, P., and Olsen, K. (2022). "High-resolution imaging of complex shallow fault zones along the July 2019 Ridgecrest ruptures," *Geophys. Res. Lett.* **49**(1), e2021GL095024, <https://doi.org/10.1029/2021gl095024>.
- Zipfel, G. G., and DeSanto, J. A. (1972). "Scattering of a scalar wave from a random rough surface: A diagrammatic approach," *J. Math. Phys.* **13**, 1903–1911.